Asymmetric Carbon Nanohorn Enabled Soft Capacitors with High Power Density and Ultra-Low Cutoff Frequency

Benxuan Li, Shijie Zhan, Haolan Wang, Bo Hou, and Gehan A. J. Amaratunga*

Flexible capacitors are a promising power source for foldable and biological electronic devices. Although various materials and device structures have been explored, they are still limited by low energy densities and slow rate capabilities compared to their rigid counterparts. Here, asymmetric carbon nanohorns are proposed as an active material to fabricate flexible solid-state carbon wire (CW)-based electrochemical supercapacitors (ss-CWECs) which exhibit high power density and ultra-low cutoff frequency. By controlling the electric arc reaction at low temperature (77 K), asymmetric single-wall carbon nanohorns (SWCNHs) are synthesized with high yield. Based on microscopy and electrochemical characterization, the fundamental reaction mechanism in polyvinyl-based electrolyte system is elucidated, as being associated with deprotonation reaction at acid, base, and elevated temperature conditions. Additionally, by using activated carbon, multi-walled carbon nanotubes, and SWCNHs as hybrid electrode materials (5:1:1), remarkable specific length capacitance of 48.76 mF cm^{-1} and charge–discharge stability (over 2000 times cycles) of ss-CWECs are demonstrated, which are the highest reported to date. Furthermore, a high-pass filter for eliminating ultra-low electronic noise is demonstrated, which enables an optical Morse Code communication system to be operated. Current results confirm the SWCNHs as promising materials for high-performance soft electronics and energy storage applications.

1. Introduction

To enable fully flexible and wearable electronics, energy storage devices such as portable batteries and electrochemical supercapacitors (ESCs) which are flexible are also required.[1,2] After decades of development, ESCs have become a viable option for many energy storage applications because they exhibit distinct merits, such as higher power density and longer cycle lifetime (>100 000 cycles) when compared to conventional capacitors and batteries.[3] In particular, the solid-state electrolyte CW-based electrochemical supercapacitors (ss-CWECs) using carbon yarn or carbon fiber as the backbone[4] have been extensively studied due to their high durability and flexibility, making them suitable for energy storage devices in the next-generation wearable electronics.[5]

Carbon is a core active electrode material in electrical double-layer capacitors (EDLCs)[6] due to its high work function and hence relative inertness (high electrochemical potential). The high abundance, low toxicity, and ability to have it in high specific surface areas with good intra/inter-particle conductivity and good electrolyte accessibility are additional advantages.[7] Typically, the surface pore size, crosslinked structure, and good dispersibility of the electrode carbons are critical parameters for realizing high-performance ESCs,[8] by having high surface areas on which to facilitate the formation of Helmholtz double layers. Activated carbon (AC) has been successfully used in commercial ESCs due to its cost-effectiveness, large surface area, and electrochemical stability. However, AC has low conductivity and thus results in poor ESC performance.[9] Other forms of carbon including carbon black,[10] carbon nanotubes (CNTs),[11] graphene, and its derivatives[12] have been studied extensively as ESC electrode materials, due to their high surface area and enhanced conductivity. However, graphene and its derivatives in supercapacitors cannot be used for high current applications because their specific capacitance dramatically decreased on increasing the current density.[13] Though CNTs have been reported as effective spacers between sheets of graphene or its derivatives to improve capacitance, by suppressing irreversible agglomerates caused by strong van der Waals interactions, ESCs fabricated only with CNTs have poor performance due to small specific

B. Li, S. Zhan, Prof. G. A. J. Amaratunga
Electrical Engineering Division
Engineering Department
University of Cambridge
9 JJ Thomson Avenue, Cambridge CB3 0FA, UK
E-mail: gaja1@cam.ac.uk
Dr. H. Wang
YINGNENG New Material Technology Co. Ltd.
Hengfeng Science and Innovation Centre
Zhengzhou 450000, P. R. China
Dr. B. Hou
School of Physics and Astronomy
Cardiff University
The Parade, Cardiff CF24 3AA, UK
E-mail: houb6@cardiff.ac.uk

The ORCID identification number(s) for the author(s) of this article can be found under https://doi.org/10.1002/admt.202000372.

capacitance compared to AC.[13] On the other hand, single-wall carbon nanohorns (SWCNHs), which have an asymmetric hollow structure, exhibit high specific capacitance as well as excellent mechanical strength with negligible irreversible agglomeration.[14] However, the use of SWCNH in ESCs has not been extensive, mainly due to the specialist nature of its synthesis, and its applications in ss-CWECs have not reported hitherto.[15]

The performance of ss-CWEC is dependent on many factors, not only the electrochemical properties of the active materials but also the electrolytes and their interfaces.[16] So far, various types of solid-state polymer electrolytes have been explored in the literature.[17] Poly(vinyl alcohol) (PA) is generally considered the best option for a solid electrolyte material, due to its eco-friendly composition as well as its facile processability. However, comprehensive comparison and discussion about the fundamental physicochemical phenomena which take place inside these polymer electrolytes in general, and in particular their impact on emerging ss-CWEC performance have not been fully understood.[18]

Here, we use AC, MWCNTs, and SWCNHs on CWs as the electrode to fabricate soft ss-CWECs, which exhibit high power density and ultra-low cutoff frequency. We demonstrate a facile carbon electric arc reaction under liquid nitrogen to fabricate SWCNHs at low-cost and large-scale. Based on systematic studies of ss-CWEC fabricated by PA at the acid, base, and elevated working temperature conditions, we elucidate the fundamental chemical reaction mechanisms during the electrochemically coupled deprotonation reaction. By employing AC, multi-walled CNT, and single-walled carbon nanohorns (AC/MWCNTs/SWCNHs) as hybrid electrode material in ss-CWECs, we demonstrate remarkable specific length capacitance and excellent cycling reliability going beyond results reported to date. We show that as-prepared ss-CWEC can provide energy to power an electronic system, but also can act as a high-pass filter to eliminate ultra-low frequency electronic noise. Finally, an integrated, active Morse Code light system is demonstrated to verify the reliability and potential application of ss-CWEC in soft electronics.

2. Results and Discussion

2.1. SWCNHs Synthesis and Morphology Characterization

SWCNHs were produced by an arc discharge method via immersed carbon in liquid nitrogen.[19] As shown in **Figure 1**, an arc was triggered in between a 6 mm diameter carbon rod, which was working as the anode and a 30 mm diameter carbon rod acting as the cathode. The discharge current and voltage were 600 A and 20 V, respectively. Liquid nitrogen was introduced into the reaction cylinder as the quenching media, and both carbon electrodes were submerged into it. The process was automatically controlled by feeding the anodic carbon rod to keep a sustainable arc, and the consumption rate of the carbon rod is ≈10 g min^{-1}. At the end of the synthesis, the as-produced SWCNHs were collected and oxidized at 550 °C for 1 h under an air atmosphere.

SWCNH is a horn-like graphitic allotrope, closely caged sp^2-bonded carbon atoms in a hexagonal curved sheet-like structure induced by pentagonal and heptagonal defects, typically with 2–5 nm diameter and 40–50 nm tube length.[20] Although their atomic structures are analogous to SWCNTs, SWCNHs generally form unique asymmetric dahlia-like, bud-like, and seed-like morphology with high electrical conductivity, as well as high specific surface area as shown in **Figure 2**a.[21] The TEM pictures of SWCNHs in Figure 2b,c show their interesting dahlia-like feature which protrudes from the aggregate surface and bud-like structure developing inside nanoparticles. Horn openings of SWCNHs are 3–5 nm in width, and it decreases to 1–2 nm curvature at the horn tips. The major differences between SWCNHs and SWCNTs are related to the shape and size. The diameter of SWCNHs is significantly larger than that of SWCNTs and it is possible to control opening of nano windows at both the tips and sidewalls of SWCNHs. For instance, SWCNHs opening hole sizes can exceed 2 nm.[22]

2.2. Mechanistic Studies of Deprotonation Reactions in Polymer Electrolyte-Based ss-CWEC

Excellent adhesion of polymer electrolytes to electrodes is one of the prerequisites for acceptable electrochemical performance in ESCs through the effective area of the double-layers being increased, resulting in larger electrode capacitance.[23] As shown in **Figure 3**a, besides the active electrode material coating (e.g., ACs, SWCNHs, or MWCNTs), CW electrodes (diameter ≈500 um) usually need to be brushed with as-prepared PA electrolyte multiple times, in order to suppress leakage current as well as enhance the ion mobilities.[24] The diameter of the whole ss-CWEC (Figure 3b,c) is about 1 mm, and the overall working length is around 5 cm (Figure S1, Supporting Information).

To assess the adhesion of polymer electrolytes to the ss-CWEC electrodes, we prepared three types of electrolytes composed of PA, PA/HP$_3$O$_4$, and PA/KOH. **Figure 4**a–c show surface morphology images of ss-CWEC with different electrolyte coatings. Noticeably the smooth coverage of ss-CWEC surface can be realized with PA/KOH electrolyte. In contrast, aggregates, voids, and uneven coverage of ss-CWEC can be observed on PA-only, and PA/H$_3$PO$_4$ coated samples. This nonuniformity would cause poor contact between interfaces of electrolyte and electrode materials, leading to high equivalent series resistance (ESR), lower capacitance, poor power density, and small energy density in the final ss-CWECs.[25]

To further explore and explain different surface morphology with the three different electrolyte materials, contact angle measurements were carried out on PA, PA/H$_3$PO$_4$, and PA/KOH thin films. As shown in Figure 4d–f, the contact angles θ for the PA, PA/H$_3$PO$_4$, and PA/KOH samples changed from 49.41° to 43.39° and 17.22°, respectively, which indicates the wire surface became increasingly hydrophilic. It should be noted that atomic force microscopy analysis (Figure S2, Supporting Information) shows that the root-mean-square roughness of PA, PA/H$_3$PO$_{4m}$, and PA/KOH films are about 13.07, 17.43, and 10.26 nm, respectively, which are well below the lower limits of surface roughness that will affect surface wettability.[26] As a result, the effect of the surface roughness appears to be negligible, and the hydrophilic and hydrophobic characteristics are attributed to the electrolyte materials themselves (see
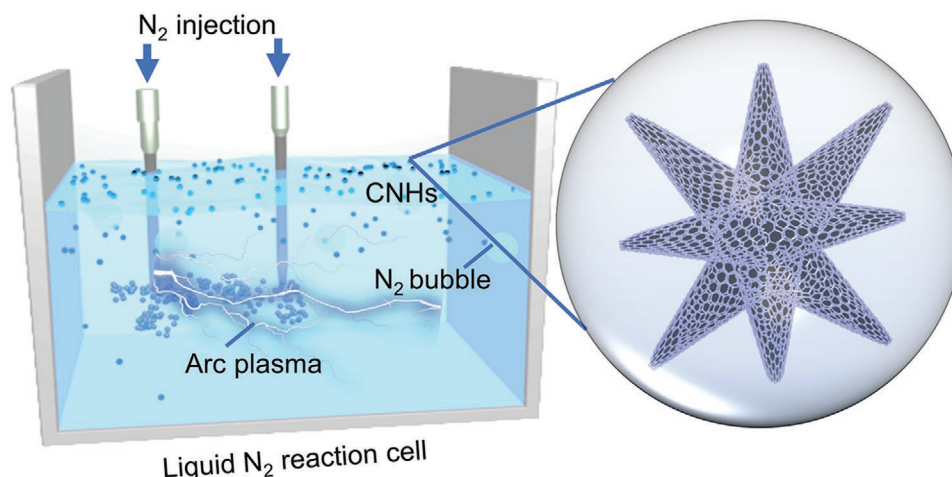
**ADVANCED
SCIENCE NEWS**
www.advancedsciencenews.com

**ADVANCED
MATERIALS
TECHNOLOGIES**
www.advmattechnol.de

Figure 1. Schematic of the electric arc method for the synthesis of SWCNHs in the liquid nitrogen atmosphere.

SEM images in Figure S3, Supporting Information). According to the thermodynamics of polymer surface reconstruction, the polarity of the surface contacting medium tends to drive the free energy state to its lowest level, and reorientation of hydroxyl groups at the membrane surface can affect their surface energy and polarities.[27] Therefore, the increasing hydrophilicity in PA, PA/H_3PO_4, and PA/KOH films are likely to be driven by the reorientation of hydroxyl groups in PA or chemical reactions which they undergo in acid or base environments. Indeed, as highlighted in the insets of Figure 4d–f, the pure PA and PA/H_3PO_4 are transparent hydrogels, while the PA/KOH hydrogels exhibit a brownish color.

Fourier-transform infrared spectroscopy (FTIR) was utilized to investigate the chemical reaction in the solid-state PA, PA/H_3PO_4 and PA/KOH electrolytes at room temperature. The FTIR spectra were normalized, and major vibration bands associated with chemical groups are presented in **Figure 5**. The broad bands between 3500 and 3200 cm^{-1} in Figure 5a, are assigned to the stretching O−H from the intermolecular and intramolecular hydrogen bonds.[28] Besides two peaks between 3000 and 2900 cm^{-1}, refer to the C−H symmetric stretching

and C−H asymmetric stretching from alkyl groups in PA. Other peaks at 1430, 1330, and 850 cm^{-1} are due to the CH_2 wagging, C−OH plane bending and C−H rocking, respectively. In contrast to FTIR spectra of room temperature PA (PART), two sharp peaks at 1150 and 950 cm^{-1} can be found in PA with H_3PO_4 loading, which is associated with C=C alkene bending. Similarly, when PA is loaded with KOH, variation occurs in the FTIR spectra with the appearance of two noticeable signals peaking at 1450 and 1350 cm^{-1}, which is related to CH_2 moiety.[29] Furthermore, the degree of crystallinity can be evaluated from FTIR spectra through the peak at 1141 cm^{-1}.[30] Interestingly, this peak can be seen in the case of PA/KOH, while none appears on PA and PA/H_3PO_4 room temperature samples. This demonstrates that PA treated with KOH exhibits more crystallized morphology, which is consistent with x-ray powder diffraction results (Figure S4, Supporting Information).

The processing and operating temperature of an electrolyte can influence the performance of ESCs, as many electrochemical or chemical reactions are closely related to temperature.[31] It should be noted that the intensity of the O−H stretching peak at 3350 cm^{-1} decreased after the pure PA film was annealed
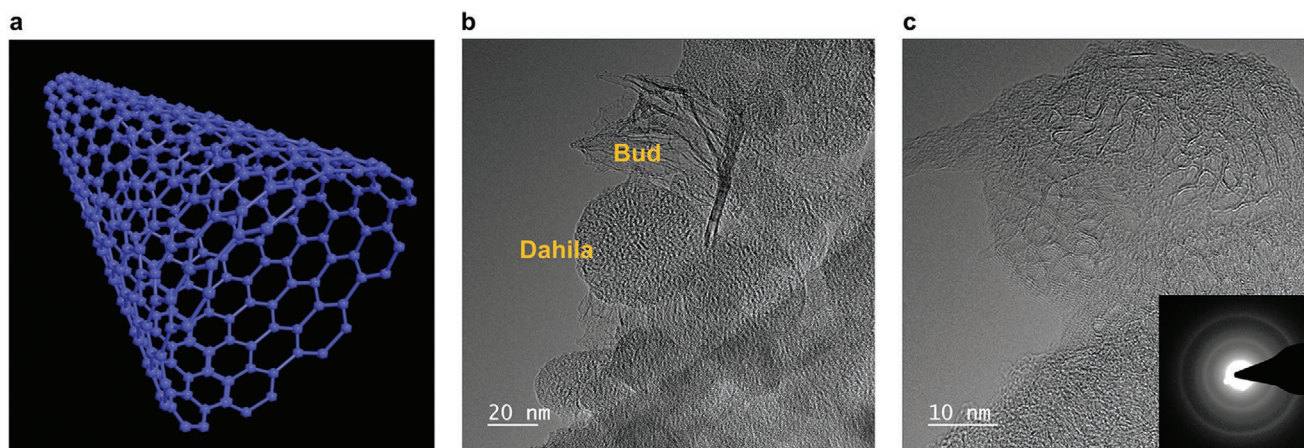

Figure 2. a) Schematic illustration of SWCNHs. b) TEM image of SWCNHs with bud-like and dahlia-like aggregates at 20 nm scale bar. c) TEM image of SWCNHs with bud-like and dahlia-like aggregates at 10 nm scale bar. Inset: Selected area electron diffraction (SEAD) result of SWCNHs.
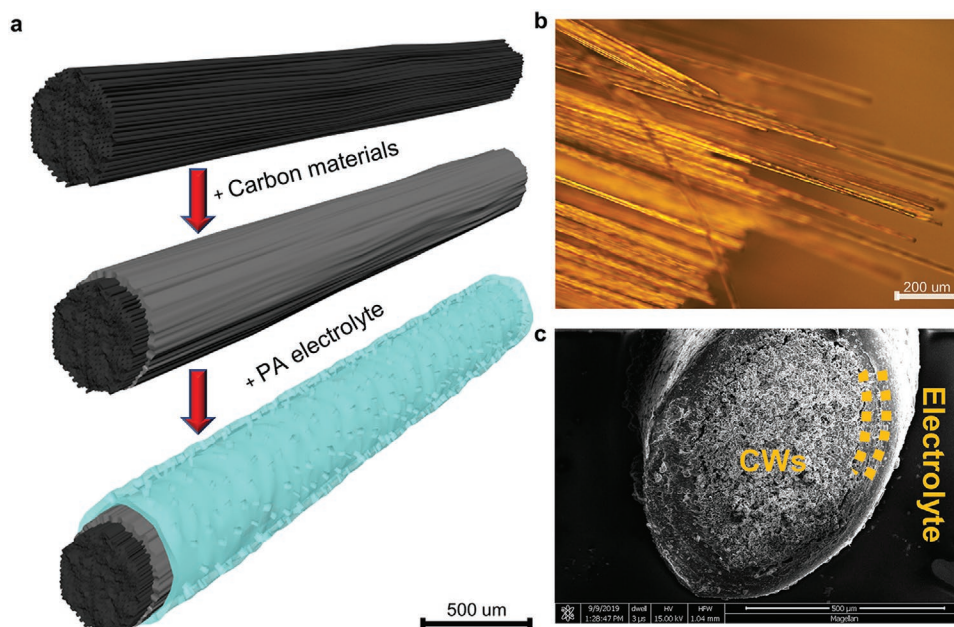
**ADVANCED
SCIENCE NEWS**
www.advancedsciencenews.com

**ADVANCED
MATERIALS
TECHNOLOGIES**
www.advmattechnol.de

Figure 3. a) Schematic illustration of the fabrication process of ss-CWECs. b) Optical image of CWs. c) SEM cross-section image of single ss-CWECs with PA electrolyte coating. The core is the CWs, and the dashed line highlighted the thickness of solid-state electrolyte.

at 90 °C for 2 h (highlighted in Figure 5a). This observation can be explained by the reduction of hydrogen bonds, as water is lost in the process of heating. Apart from this, no other noticeable changes and shifts of peaks are seen, indicating no heating-induced chemical reaction occurred except for water vaporization. In Figure 5b, intensity shift can be seen in the range of 1150–950 cm^{-1}, in correlation with C=C alkane bending (as discussed above), while the rest of the spectra remain unchanged, regardless of processing via air drying or

heating at 90 °C (highlighted in Figure 5b). Furthermore, the peak intensity variation between 995 and 960 cm^{-1} is related to the *cis–trans* isomerism that happens during a dehydration reaction within the acid environment(*cis–trans* isomerism reaction is shown in **Scheme 1**).[2] In contrast, when PA is put in a base environment, sharp doublet peaks appear in the range of 1450–1350 cm^{-1}, implying the possible formation of O−H bending in aldehyde.[32] An increase of temperature will only influence peak intensity, namely proportion of the reaction
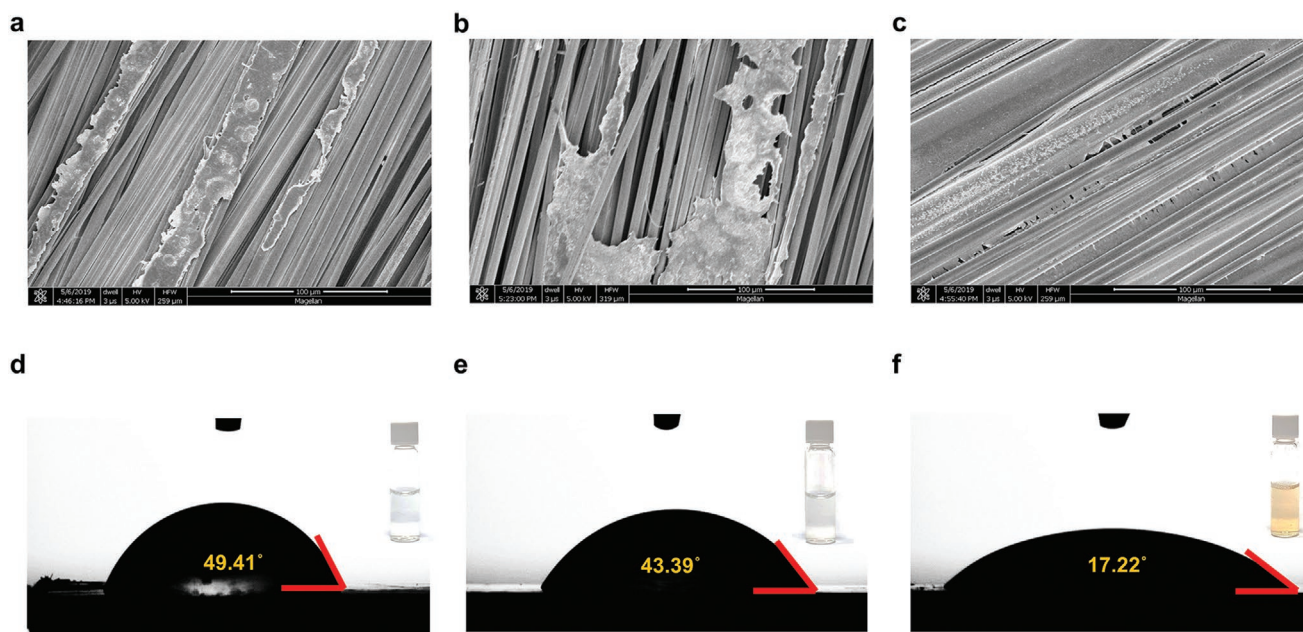

Figure 4. SEM images and water contact angle pictures of ss-CWECs with different coatings of solid-state electrolytes on carbon fibers. a,d) PA, b,e) PA/H$_3$PO$_4$, and c,f) PA/KOH thin films, with insets displaying transparent PA, PA/H$_3$PO$_4$, and brownish PA/KOH solution, respectively.

**ADVANCED
SCIENCE NEWS**
www.advancedsciencenews.com

**ADVANCED
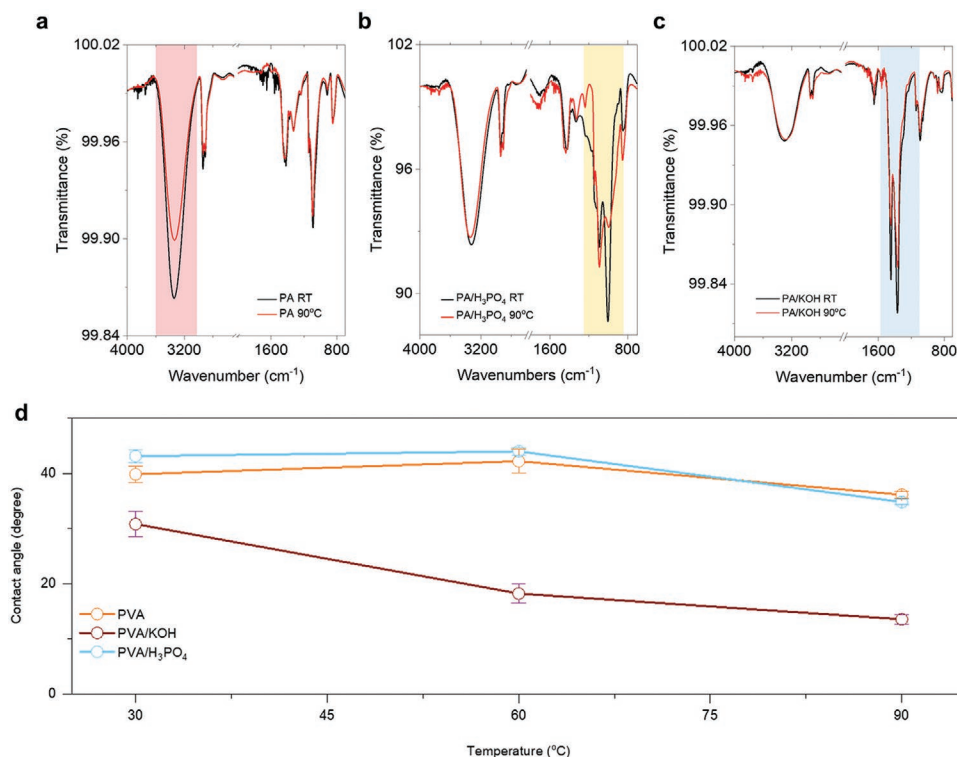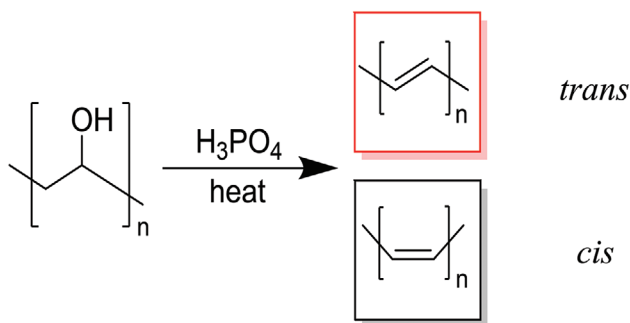MATERIALS
TECHNOLOGIES**
www.advmattechnol.de

Figure 5. Normalized FTIR spectra of PA in different acid and base conditions. a) PA, b) PA/H$_3$PO$_4$, and c) PA/KOH thin films processed at room temperature and 90 °C. d) Water contact angle results as a function of heating time.

product (highlighted in Figure 5c). For PA and PA/H$_3$PO$_4$ samples, the value of contact angle increased with increasing heating temperature from 30 to 60 °C; however, these values then dropped sharply with higher temperature up to 90 °C. Hence, in the temperature range from 30 to 60 °C, surface wettability of PA and PA/H$_3$PO$_4$ thin films will not change significantly. Still, the surface will become more hydrophilic when films are further heated to a higher temperature. As mentioned above, double bonds are formed in PA/H$_3$PO$_4$ due to the deprotonation reaction and since double bonds are naturally more hydrophobic than hydroxyl groups, production of double bonds in PA/H$_3$PO$_4$ reactions can be the explanation for relatively higher hydrophilicity shown in the case of PA/H$_3$PO$_4$ than pure PA. Moreover, during the deprotonation reaction with H$_3$PO$_4$, production of H$_2$O compensates for water loss from heating, which
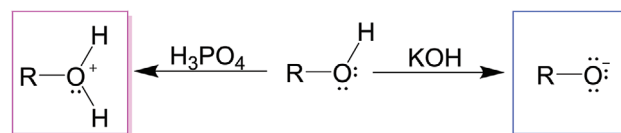
is consistent with findings in the TGA results (Figure S5, Supporting Information). Therefore, PA/H$_3$PO$_4$ becomes more hydrophilic than pure PA at 90 °C. Nevertheless, in terms of PA/KOH, it is observed that the film surface is initially more hydrophilic than that in PA and PA/H$_3$PO$_4$ thin films, and its hydrophilicity is enhanced when the temperature is raised continuously to 60 and 90 °C. As shown in the plausible reaction scheme in **Scheme 2**, during the PA deprotonation reaction with a strong acid, the hydroxyl group in PA donates two electrons to H from the acid reagent, resulting in an alkyloxonium before conversion into a carbon cation, which is then attacked by deprotonated acid to form a double bond. On the other hand, free state radicals will be produced during the PA deprotonation reaction with a strong base, together with free state K$^+$ and OH$^-$ to enhance the resulting ionic conductivity and polarity.

2.3. Electrochemical Properties of the PA/KOH and PA/H$_3$PO$_4$ Electrolyte and Corresponding ss-CWECs

Following the investigation on wettability, structure, morphology, and thermal stability in PA, PA/H$_3$PO$_4$, and PA/KOH,

Scheme 1. Reaction scheme shows the *cis–trans* isomerism reaction route in PA/H$_3$PO$_4$.

Scheme 2. Reaction scheme shows the deprotonation reaction of PA under acid or base conditions.

**ADVANCED
SCIENCE NEWS**

www.advancedsciencenews.com

**ADVANCED
MATERIALS
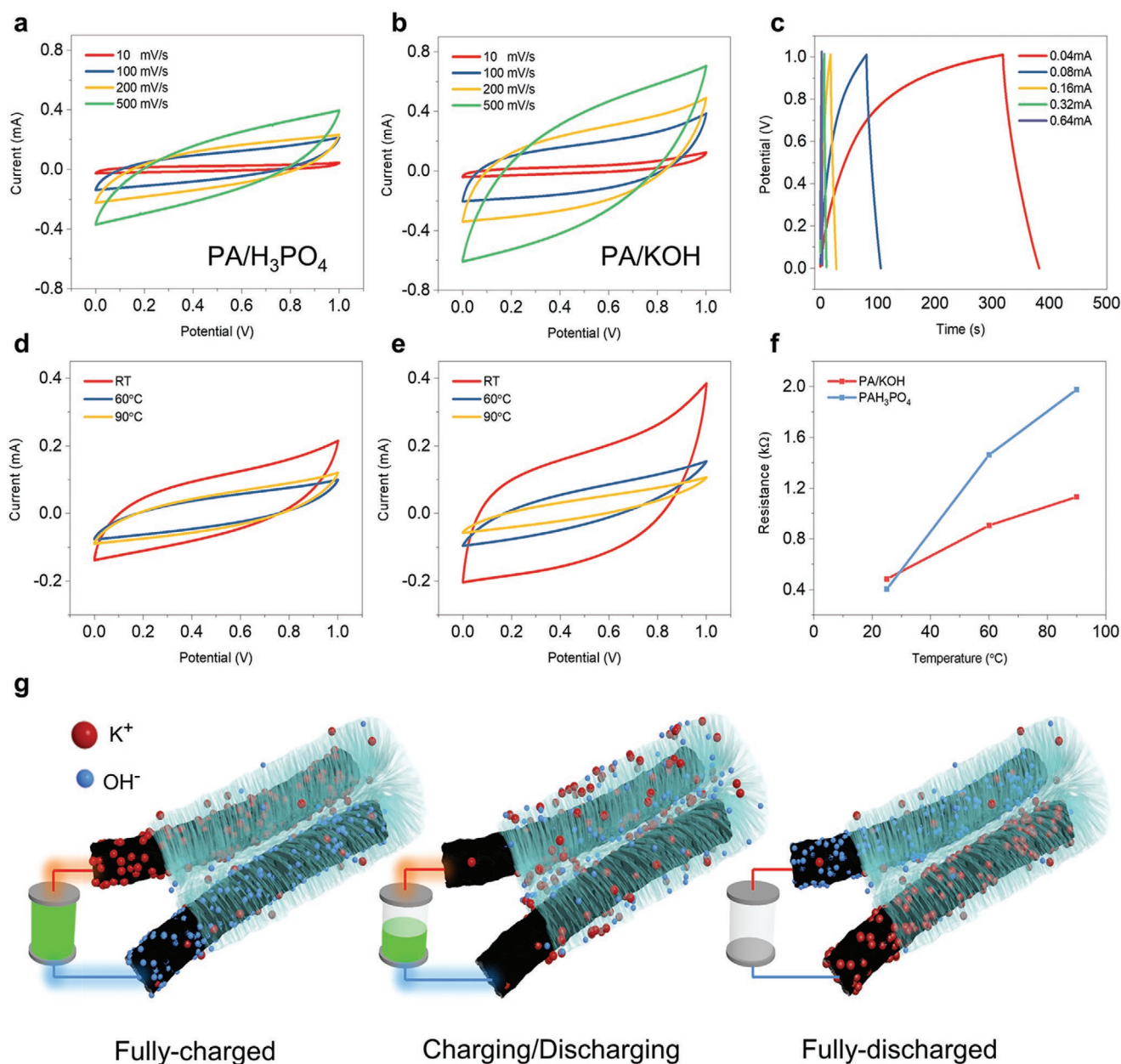TECHNOLOGIES**

www.advmattechnol.de

Figure 6. a) CVs taken at 10, 100, 200, and 500 mV s^{-1} with PA/H$_3$PO$_4$ devices. b) CVs taken at 10, 100, 200, and 500 mV s^{-1} with PA/KOH devices. c) GCD curves of PA/KOH devices at various current densities. d) CVs took at 100 mV s^{-1} after PA/H$_3$PO$_4$ devices were processed at room temperature, 60 and 90 °C. e) CVs took at 100 mV s^{-1} after PA/KOH devices were processed at room temperature, 60 and 90 °C. f) Calculated resistance values of PA/H$_3$PO$_4$ and PA/KOH ESCs when processed at room temperature, 60 and 90 °C. g) Schematic illustration of charge transfer dynamics in ss-CWECs at fully-charged, charging/discharging, and fully-discharged status.

ss-CWECs were fabricated, and their electrochemical performance was characterized. This allows a correlation between the internal physical and chemical processes and electrochemical device behavior. Representative CV curves of devices with PA/H$_3$PO$_4$ and PA/KOH electrolytes at various scan rates are given in **Figure 6**a,b. The CV curves in Figure 6a,b show large enclosed areas which indicate large charge storage capacities. Additionally, significant enlargement in the CV curves can be observed as scan rate increases from 10 to 500 mV s^{-1}. Although the same increment trend is also seen in Figure 6a, current values at all scan rates are all below that in PA/KOH devices in Figure 6b. To further compare devices with two different electrolytes, specific length capacitance is calculated from the CV curves in Figure 6a,b. For PA/H$_3$PO$_4$, values of specific length capacitance decrease from 0.029, 0.015, and 0.010 to 0.006 mF cm^{-1} when the CV scan rates increase from 10, 100, and 200 to 500 mV s^{-1}. For PA/KOH, specific length capacitance drops from 0.042, 0.026, and 0.019 to 0.011 mF cm^{-1} with the same scan rates. Therefore, it is evident that specific length capacitance of ss-CWECs is doubled when PA/KOH

**ADVANCED
SCIENCE NEWS**
www.advancedsciencenews.com

**ADVANCED
MATERIALS
TECHNOLOGIES**
www.advmattechnol.de

replaces the PA/H_3PO_4 as the coating electrolyte. To further evaluate the electrochemical characteristics of as-obtained ss-CWECs, galvanostatic charge–discharge (GCD) measurement and temperature-dependent CV analysis were conducted (Figure 6c–e; Figure S6, Supporting Information). Noticeably, PA/KOH ss-CWECs exhibit two times higher specific capacitance than PA/H_3PO4 at room temperature though both system exhibit inferior performance at elevated temperature. It should be noted that GCD curves of PA/KOH ss-CWECs exhibit low Columbic efficiency, especially at low charging/discharging current, which is because of the low charge storage characteristics of carbon fibers. Figure 6f summarizes the bulk resistance for all ss-CWECs which are extracted from electrochemical impedance spectroscopy (EIS of ss-CWECs with PA/H_3PO_4 and PA/KOH are given in Figure S7, Supporting Information).[33] In both cases, overall bulk resistance increases with rising environmental temperature, but at a relatively higher rate for PA/H_3PO_4 cells compared to PA/KOH cells, although they show similar resistance at room temperature. The improved performance of ss-CWECs with the replacement of PA/H_3PO_4 by PA/KOH originates from better adhesion as well as enhanced charge transfer dynamics inside the ion conductive medium.[34] As shown in Figure 6g, ss-CWECs are EDLCs, where electrical charge is stored at the electrode and electrolyte interface.[35] Therefore, K^+ cations and OH^- anions are bound on the ss-CWECs surfaces during adsorption when the cell is fully charged. On the other hand, K^+ cations and OH^- anions exchange their binding CWEC electrodes when the same device is completely discharged. Amid these two states, ions are under desorption conditions where solvated cations and anions are establishing equilibrium states from free states, made available by external charging and discharging forces. As seen in the Scheme 2, within PA/H_3PO_4 medium, olefin moieties will be generated in PA deprotonation reactions, but radicals will be the main product in its reactions with KOH, which ultimately result in different wettability properties and thus impacts on physical electrolyte contact with electrodes. Therefore, we select PA/KOH as the electrolyte for fabricating ss-CWECs which can provide better electrochemical performance than PA/H_3PO_4.

2.4. Effect of SWCNH and MWCNT Hybrid Loadings on ss-CWECs

To elucidate which carbon material combinations will give best capacitance results, four groups of ss-CWECs were fabricated with pure AC, hybrid AC/SWCNHs, AC/MWCNTs, and AC/MWCNTs/SWCNHs at a weight ratio of 5:1 or 5:1:1, respectively. The CVs from four loading combinations are shown in **Figure 7**a. The calculated specific length capacitances (at 10 mV s^{-1}) are 16.08, 25.08, 35.71, and 48.76 mF cm^{-1} for AC, AC/SWNH, AC/MWCNTs, and AC/MWCNTs/SWNHs, respectively. It can also be seen that ss-CWECs with AC/MWCNTs/SWCNHs loading gives largest scanning area, which shows the biggest capacitance. Indeed, the specific length capacitance extracted from CV curves increases 1160 times from 0.042 mF cm^{-1} in pure ss-CWECs to 48.76 mF cm^{-1} in AC/MWCNTs/SWCNHs functionalized ss-CWECs, which is the highest value among any reported carbon-based yarn and fiber type ESCs (see detailed comparison

in Table S1, Supporting Information).[4,36] ESCs coated with AC/MWCNTs/SWCNHs at different ratios were also studied, and analysis suggests that AC/MWCNTs/SWCNHs at 5:1:1 blending ratio provides best electrochemical performance (more information about CVs and galvanostatic charge and discharge curves of the best cell are presented in Figure S8, Supporting Information). In addition to CV measurement, the EIS analysis was carried out to investigate the electrochemical properties of as-prepared ss-CWECs, as shown in Figure 7b. The ESR of the AC/SWCHNs sample is the smallest, and this indicates that the addition of SWCNHs has the main impact in increasing conductivity of hybrid carbon material (Figure S9, Supporting Information). Furthermore, the I_D/I_G ratios extracted from Raman spectra were also calculated. As shown in Figure S10, Supporting Information, the pure MWCNTs present the smallest I_D/I_G (0.842) compared to ACs (1.198) and MWCNTs (1.018), revealing the SWCHNs have a high electrical conductivity.[37]

The enhanced electrochemical performance of our hybrid carbon materials ss-CWECs is likely to be derived from two key aspects: First, the introduction of SWCNHs into AC/MWCNTs renders ss-CWECs more conductive, since voids between AC and MWCNTs will be filled with highly conductive Dahlia-like SWCNHs aggregates (Figure S11, Supporting Information). Thus, SWCNHS act as cross-linker/binder in AC and MWCNTs, filling in voids and resulting in lower ESR (Figure 7b). As illustrated in Figure 7c–e, unfilled space between AC and MWCNTs is likely to become barriers and preclude electron transfer in carbon materials, while compact SWCNHs can encompass AC and MWCNTs, leading to a higher possibility of intra- and inter-pore pathways for electron transfer. Second, the data (Figure 7a) show that when only SWNHs are combined with AC the capacitance is lower than when only MWCNTs are combined with AC. This suggests that though SWNH can act as a very effective conductive binder, it also can inhibit access to the active pores of the AC (which give it a very high equivalent surface) area. Inclusion of the MWCNTs, on the other hand, penetrates the AC and gives better ionic access to interior pores of the AC. Therefore, the combination of MWCNTs and SWNHs with AC results in the optimum EC performance. The enlarged schematic in Figure 7e highlighted the more detailed 3D structure of compactly cross-linked hybrid AC/MWCNTs/SWCNHs composites inside the coating layer of the ss-CWECs. Furthermore, AC/MWCNTs/SWCNHs are naturally hydrophilic, so there is excellent compatibility with PA/KOH electrolyte to ensure good wettability and dispersity (see dispersion inks in Figure S12, Supporting Information) between electrode–electrolyte interface (see SEM images in Figure S13, Supporting Information).

The Ragone plot derived from galvanostatic charge and discharge curves are shown in **Figure 8**a, with comparison to other reported works. It can be seen that the energy density (at 64 mA g^{-1}) of the best cell reaches 129.087 µWh cm^{-2} and power density of 16.30 mW cm^{-2}, which is the highest among all reported flexible yarn or fiber type carbon-based ESCs (see the detailed comparison in the Table S1, Supporting Information). Considering cycling stability, ss-CWECs with hybrid AC/MWCNTs/SWCNHs loading reveals excellent capacitance retention after 2000 cycles at the scan rate of 10 mV s^{-1} (Figure 8b)
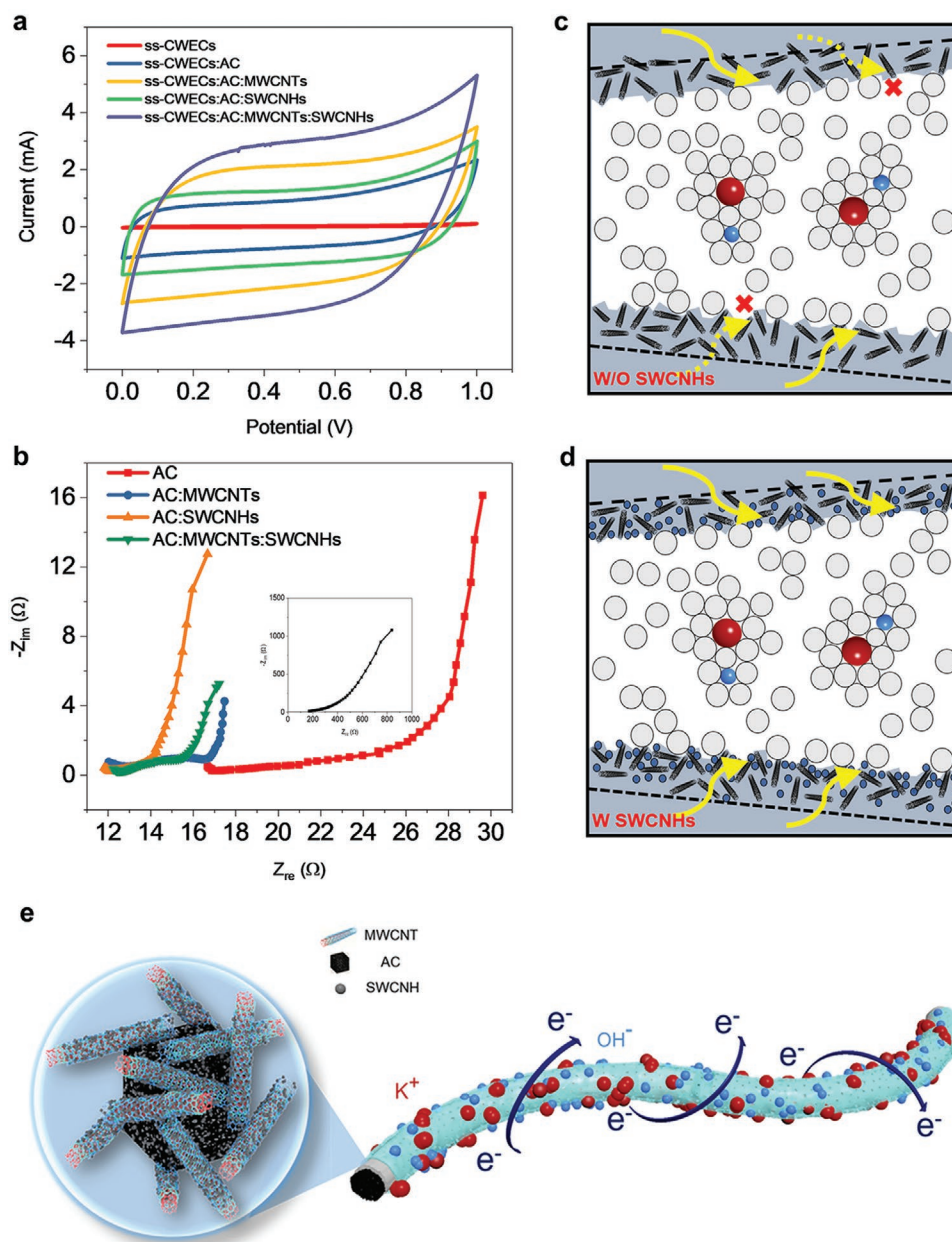
Figure 7. a) CVs (scan rate of 10 mV s^{-1}) of pure ss-CWECs and ss-CWECs with AC, AC/MWCNTs, AC/SWCNHs, and AC/MWCNTs/SWCNHs loadings. b) EIS results of ss-CWECs with different carbon material loading. Inset is EIS of pure ss-CWECs. Schematic illustrations of the interface charge transport dynamics c) without (w/o) SWCNHs, d) with (w) SWCNHs, and e) PA/KOH electrolyte encapsulated AC/MWCNTs/SWCNHs ensemble electrodes.

2.5. ss-CWECs Assembly and Application in an Internet of Things System

A thin-film transistor (TFT)-controlled current-driven LED system (**Figure 9**a) was built to demonstrate further the high specific capacitance of as-prepared ss-CWECs as a continuous power supply for an Internet of things (IoT) system. As shown in Figure 9b, an indium gallium zinc oxide TFT and a red surface-mounted light-emitting diode (SML) are integrated into a light-emitting and control-drive system. In the circuit (Figure 9a), both the TFT gate and the LED are powered by a supercapacitor which is formed of 30 cm long (in the unwound

state) ss-CWECs connected in series to give around 6 V output. A small-signal AC square waveform realized the modulation of the red light from 0 to 5 V generated from a function generator, which gave gate bias together with the supercapacitor in series. Thus, the total voltage at the gate was the linear combination of the DC and AC bias (Equation (1)):

$$V_g = V_{sup} + V_{ac} \qquad (1)$$

where V_{sup}, V_{ac}, and V_g are the DC bias from the supercapacitor, the AC bias from the function generator, and the total gate voltage, respectively. The AC bias acts to modulate the gate voltage with
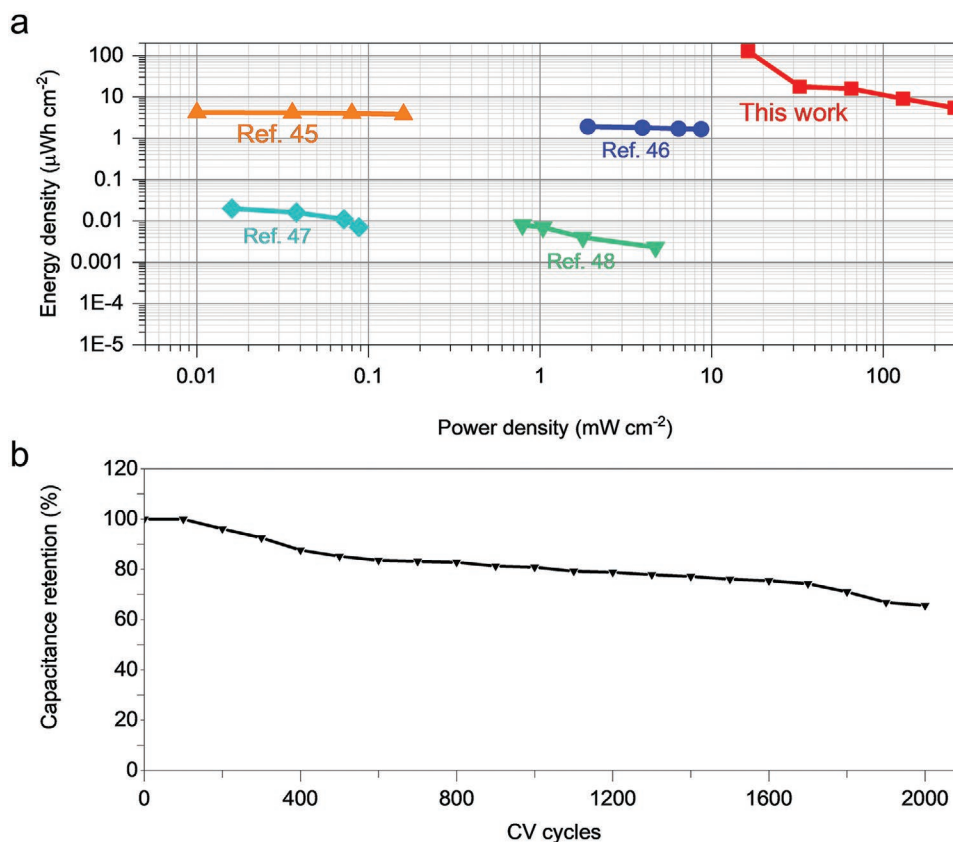
**ADVANCED
SCIENCE NEWS**
www.advancedsciencenews.com

**ADVANCED
MATERIALS
TECHNOLOGIES**
www.advmattechnol.de

Figure 8. a) Ragone plots compared with the represented previous works. b) Capacitance retention after 2000 cycles of ss-CWECs at a scan rate of 10 mV s^{-1}.

the DC offset from the supercapacitor and turn the transistor ON or OFF. Though both drain and gate are biased with the supercapacitor, the energy loss on the TFT gate is negligible due to a low gate current. Combined with the high energy density of the supercapacitor, this set-up enables the ss-CWECs to act as a DC power supply, to maintain the light intensity during operation without noticeable fading (see Video S1, Supporting Information).

It should be noted that the ss-CWECs can also play a role as an electronic filter which exhibits an ultra-low cutoff frequency, as in an ideal power supply. A high-pass filter analysis system was constructed (Figure S14, Supporting Information) to demonstrate the superior filtering characteristic of the ss-CWECs compared to the conventional capacitors. As shown in Figure 9c, the frequency response still keeps more than 85% of its original value, even at 0.1 Hz for the ss-CWECs, while the transmission of a 470 µF standard capacitor filter drops off quickly to 50% before 10 Hz as predicted by the transmission function (Equation (2))

$$T = 1 - \frac{1}{1 + 2\pi fRC} \qquad (2)$$

where R and C are the resistance and capacitance of the resistor and capacitor in the filter. T is the transmission of the filter and f stands for the frequency of the input signal. In the circuit, a 50 Ω resistor and a 470 µF electrolytic capacitor were used for a conventional high-pass filter, exhibiting a frequency response with 3 dB cutoff at 16.8 Hz (Figure 9c). For a typical RC filter, the cutoff frequency is determined by $1/2\pi RC$, where the signal ampli-

tude decays to 3 dB of the input signal amplitude. Therefore, with the ultra-high capacitance of more than 200 mF for the ss-CWECs supercapacitor, the cutoff frequency of the filter is much lower than that of the filter with the 470 µF conventional electrolytic capacitor. From this frequency response test, the concept of supercapacitor signal processing is put forward in this work, which may inspire new applications in wearable electronics such as body signal processing. For example, breath signal during sleep has a quite low frequency ≈0.2 Hz and body movement may have frequency even lower than 0.1 Hz. Therefore, our ss-CWECs not only could work as a power supply but also allows signal processing with ultralow frequency on flexible systems.

Furthermore, as highlighted in Figure 9d, by outputting the square waveform at 0.5 Hz, the red light of SML can be driven at the modulation rate. The ss-CWECs-powered current-driven LED circuit is demonstrated in active signal communication to generate an optical Morse Code (see Videos S2–S4, Supporting Information). As shown in Figure 9d, "CAM" was separately generated by setting the AC waveform according to the international encoding method, where the dash is presented by continuous lightning for 3 s, and the dot is for 1 s with 1 s-off between each signal.

3. Conclusions

In summary, PA/KOH as a solid-state electrolyte and hybrid AC/MWCNT/SWCNHs coated on a carbon fiber backbone as the electrodes are used to demonstrate soft ss-CWECs, which
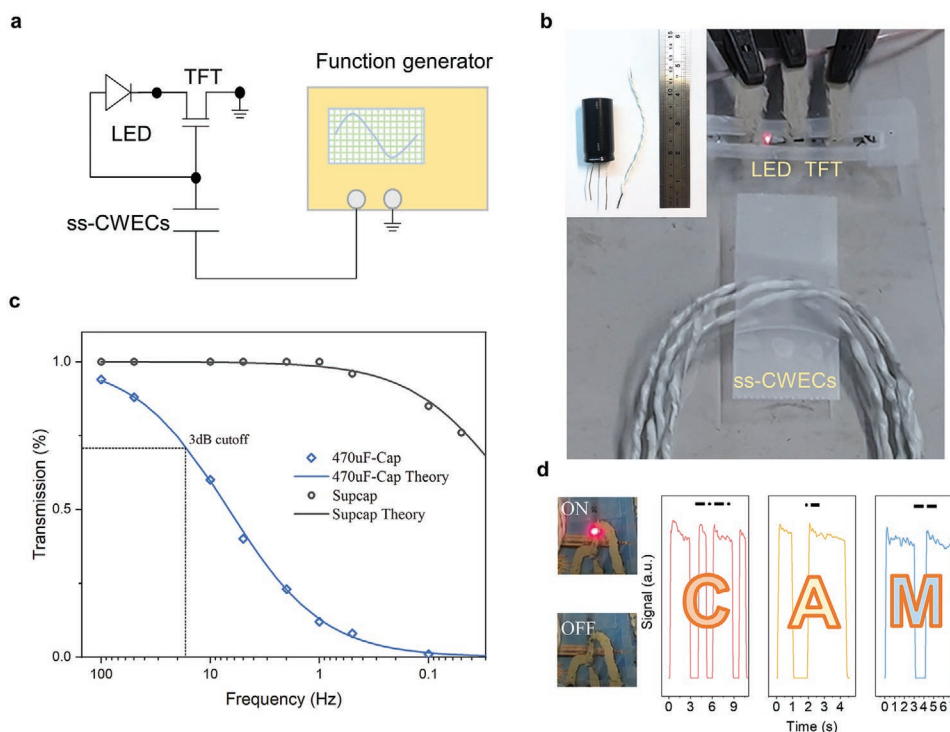
**ADVANCED
SCIENCE NEWS**
www.advancedsciencenews.com

**ADVANCED
MATERIALS
TECHNOLOGIES**
www.advmattechnol.de

Figure 9. a) An equivalent circuit diagram and b) a snapshot image of ss-CWECs powered TFT-LED. (Inset shows the size comparison of ss-CWECs and a commercial 470 µF capacitor). c) The frequency response for the high-pass RC filter using an ss-CWECs and conventional capacitor (dot for experimental data and line for theory data). d) Morse code "CAM" generated by the ss-CWECs powered circuit. The red LED lighting is enabled when the ss-CWECs bias the gate.

exhibit high-power density and ultra-low cutoff frequency. PA/KOH is chosen as the solid electrolyte to construct ss-CWECS since it is prone to form a hydrophilic interface and thus better adhesion to CWs. Based on systematic spectroscopy, microscopy, and interface analysis, we further clarify and expand the fundamental understanding of PA deprotonation reaction in ss-CWECs at the acid, base, and elevated working temperature conditions. By employing AC/MWCNTs/SWCNHs (5:1:1) as hybrid electrode materials in ss-CWECs, we demonstrate a remarkable specific length capacitance of 48.76 mF cm^{-1} (at 10 mV s^{-1}) with excellent charge–discharge stability (>70% remaining capacitance after over 2000 times charge–discharge cycling test). We further show that the as-prepared ss-CWECs can provide sufficient power for LED light modulation and enable a high-pass filter to eliminate ultra-low electronic noise. The use of the ss-CWEC as a supercapacitor power supply in a representative IoT soft electronics system is also verified.

Conflict of Interest

The authors declare no conflict of interest.

[1] a) Z. Chen, D. Zhang, X. Wang, X. Jia, F. Wei, H. Li, Y. Lu, *Adv. Mater.* **2012**, *24*, 2030; b) Z. Liu, F. Mo, H. Li, M. Zhu, Z. Wang, G. Liang, C. Zhi, *Small Methods* **2018**, *2*, 1800124; c) B. Hou, M. Sohn, Y.-W. Lee, J. Zhang, J. I. Sohn, H. Kim, S. Cha, J. M. Kim, *Nano Energy* **2019**, *62*, 764.

[2] S. Zhan, S. Han, S. Y. Bang, B. Li, Y. T. Chun, B. Hou, J. M. Kim, *Phys. Status Solidi* **2020**, *217*, 1900832.

[3] a) R. Kötz, M. Carlen, *Electrochim. Acta* **2000**, *45*, 2483; b) P. Simon, Y. Gogotsi, *Nat. Mater.* **2008**, *7*, 845; c) A. Burke, *Electrochim. Acta* **2007**, *53*, 1083.

[4] a) S. Zhai, W. Jiang, L. Wei, H. E. Karahan, Y. Yuan, A. K. Ng, Y. Chen, *Mater. Horiz.* **2015**, *2*, 598; b) V. T. Le, H. Kim, A. Ghosh, J. Kim, J. Chang, Q. A. Vu, D. T. Pham, J.-H. Lee, S.-W. Kim, Y. H. Lee, *ACS Nano* **2013**, *7*, 5940; c) Q. Meng, K. Wang, W. Guo, J. Fang, Z. Wei, X. She, *Small* **2014**, *10*, 3187; d) Y. Huang, H. Hu, Y. Huang, M. Zhu, W. Meng, C. Liu, Z. Pei, C. Hao, Z. Wang, C. Zhi, *ACS Nano* **2015**, *9*, 4766; e) J. Ren, W. Bai, G. Guan, Y. Zhang, H. Peng, *Adv. Mater.* **2013**, *25*, 5965.

[5] a) A. González, E. Goikolea, J. A. Barrena, R. Mysyk, *Renewable Sustainable Energy Rev.* **2016**, *58*, 1189; b) C. Meng, C. Liu, L. Chen, C. Hu, S. Fan, *Nano Lett.* **2010**, *10*, 4025; c) G. Xiong, C. Meng, R. G. Reifenberger, P. P. Irazoqui, T. S. Fisher, *Adv. Energy Mater.* **2014**, *4*, 1300515; d) F. Mo, G. Liang, Z. Huang, H. Li, D. Wang, C. Zhi, *Adv. Mater.* **2020**, *32*, 1902151; e) G. Liang, F. Mo, Q. Yang, Z. Huang, X. Li, D. Wang, Z. Liu, H. Li, Q. Zhang, C. Zhi, *Adv. Mater.* **2019**, *31*, 1905873; f) B. Li, J. Lu, J. Feng, J. Zhang, P. M. Smowton, J. I. Sohn, I.-K. Park, H. Zhong, B. Hou, *J. Mater. Chem. C* **2020**, https://doi.org/10.1039/d0tc01349h.

[6] a) M. J. Bleda-Martínez, J. A. Maciá-Agulló, D. Lozano-Castelló, E. Morallón, D. Cazorla-Amorós, A. Linares-Solano, *Carbon* **2005**, *43*, 2677; b) W. Li, D. Chen, Z. Li, Y. Shi, Y. Wan, G. Wang, Z. Jiang, D. Zhao, *Carbon* **2007**, *45*, 1757; c) M. Inagaki, H. Konno, O. Tanaike, *J. Power Sources* **2010**, *195*, 7880; d) L. Wei, G. Yushin, *Nano Energy* **2012**, *1*, 552.

[7] a) B. Xu, F. Wu, R. Chen, G. Cao, S. Chen, Z. Zhou, Y. Yang, *Electrochem. Commun.* **2008**, *10*, 795; b) C. Merlet, B. Rotenberg, P. A. Madden, P.-L. Taberna, P. Simon, Y. Gogotsi, M. Salanne, *Nat. Mater.* **2012**, *11*, 306; c) F. Xu, Z. Tang, S. Huang, L. Chen, Y. Liang, W. Mai, H. Zhong, R. Fu, D. Wu, *Nat. Commun.* **2015**, *6*, 7221.

[8] J. Chmiola, G. Yushin, Y. Gogotsi, C. Portet, P. Simon, P. L. Taberna, *Science* **2006**, *313*, 1760.

[9] J. Yan, Q. Wang, T. Wei, Z. Fan, *Adv. Energy Mater.* **2014**, *4*, 1300816.

[10] G. Wang, X. Sun, F. Lu, H. Sun, M. Yu, W. Jiang, C. Liu, J. Lian, *Small* **2012**, *8*, 452.

[11] a) M. Kaempgen, C. K. Chan, J. Ma, Y. Cui, G. Gruner, *Nano Lett.* **2009**, *9*, 1872; b) P. Hiralal, H. Wang, H. E. Unalan, Y. Liu, M. Rouvala, D. Wei, P. Andrew, G. A. J. Amaratunga, *J. Mater. Chem.* **2011**, *21*, 17810; c) J. Sun, Y. Huang, C. Fu, Z. Wang, Y. Huang, M. Zhu, C. Zhi, H. Hu, *Nano Energy* **2016**, *27*, 230.

[12] a) X. Li, Y. Tang, J. Song, W. Yang, M. Wang, C. Zhu, W. Zhao, J. Zheng, Y. Lin, *Carbon* **2018**, *129*, 236; b) G. Wu, P. Tan, X. Wu, L. Peng, H. Cheng, C.-F. Wang, W. Chen, Z. Yu, S. Chen, *Adv. Funct. Mater.* **2017**, *27*, 1702493.

[13] M. Lu, G. Wang, B. Li, J. Chen, J. Zhang, Z. Li, B. Hou, *Phys. Chem. Chem. Phys.* **2019**, *21*, 22283.

[14] S. Iijima, M. Yudasaka, R. Yamada, S. Bandow, K. Suenaga, F. Kokai, K. Takahashi, *Chem. Phys. Lett.* **1999**, *309*, 165.

[15] a) A. Izadi-Najafabadi, T. Yamada, D. N. Futaba, M. Yudasaka, H. Takagi, H. Hatori, S. Iijima, K. Hata, *ACS Nano* **2011**, *5*, 811; b) K. P. Annamalai, J. Gao, L. Liu, J. Mei, W. Lau, Y. Tao, *J. Mater. Chem. A* **2015**, *3*, 11740.

[16] S. Zhang, N. Pan, *Adv. Energy Mater.* **2015**, *5*, 1401401.

[17] a) N. A. Choudhury, S. Sampath, A. K. Shukla, *Energy Environ. Sci.* **2009**, *2*, 55; b) H. Gao, K. Lian, *RSC Adv.* **2014**, *4*, 33091;

c) X. Cheng, J. Pan, Y. Zhao, M. Liao, H. Peng, *Adv. Energy Mater.* **2018**, *8*, 1702184.

[18] a) D. Kalpana, N. G. Renganathan, S. Pitchumani, *J. Power Sources* **2006**, *157*, 621; b) X. Yang, F. Zhang, L. Zhang, T. Zhang, Y. Huang, Y. Chen, *Adv. Funct. Mater.* **2013**, *23*, 3353; c) Y. Huang, M. Zhong, F. Shi, X. Liu, Z. Tang, Y. Wang, Y. Huang, H. Hou, X. Xie, C. Zhi, *Angew. Chem., Int. Ed.* **2017**, *56*, 9141.

[19] H. Wang, M. Chhowalla, N. Sano, S. Jia, G. A. J. Amaratunga, *Nanotechnology* **2004**, *15*, 546.

[20] U. Gulzar, T. Li, X. Bai, M. Colombo, A. Ansaldo, S. Marras, M. Prato, S. Goriparti, C. Capiglia, R. Proietti Zaccaria, *ACS Appl. Mater. Interfaces* **2018**, *10*, 5551.

[21] N. Karousis, I. Suarez-Martinez, C. P. Ewels, N. Tagmatarchis, *Chem. Rev.* **2016**, *116*, 4850.

[22] a) S. Zhu, G. Xu, *Nanoscale* **2010**, *2*, 2538; b) J. Suehiro, N. Sano, G. Zhou, H. Imakiire, K. Imasaka, M. Hara, *J. Electrost.* **2006**, *64*, 408; c) K. Urita, S. Seki, S. Utsumi, D. Noguchi, H. Kanoh, H. Tanaka, Y. Hattori, Y. Ochiai, N. Aoki, M. Yudasaka, S. Iijima, K. Kaneko, *Nano Lett.* **2006**, *6*, 1325.

[23] a) C. Zhong, Y. Deng, W. Hu, J. Qiao, L. Zhang, J. Zhang, *Chem. Soc. Rev.* **2015**, *44*, 7484; b) L. L. Zhang, X. S. Zhao, *Chem. Soc. Rev.* **2009**, *38*, 2520.

[24] a) P. N. Gupta, K. P. Singh, *Solid State Ionics* **1996**, *86-88*, 319; b) S. Rajendran, O. Mahendran, *Ionics* **2001**, *7*, 463.

[25] C. Portet, P. L. Taberna, P. Simon, E. Flahaut, C. Laberty-Robert, *Electrochim. Acta* **2005**, *50*, 4174.

[26] a) B. Zuo, Y. Hu, X. Lu, S. Zhang, H. Fan, X. Wang, *J. Phys. Chem. C* **2013**, *117*, 3396; b) H. J. Busscher, A. W. J. van Pelt, P. de Boer, H. P. de Jong, J. Arends, *Colloids Surf.* **1984**, *9*, 319.

[27] a) S. Khongtong, G. S. Ferguson, *J. Am. Chem. Soc.* **2001**, *123*, 3588; b) J. A. Crowe, J. Genzer, *J. Am. Chem. Soc.* **2005**, *127*, 17610; c) X. Wang, X. Wang, Z. Chen, *Polymer* **2007**, *48*, 522.

[28] a) H. Maeda, T. Kawai, S. Sekii, *J. Polym. Sci.* **1959**, *35*, 288; b) H. S. Mansur, C. M. Sadahira, A. N. Souza, A. A. P. Mansur, *Mater. Sci. Eng., C* **2008**, *28*, 539.

[29] S. K. Mallapragada, N. A. Peppas, P. Colombo, *J. Biomed. Mater. Res.* **1997**, *36*, 125.

[30] H. Fei, C. Yang, H. Bao, G. Wang, *J. Power Sources* **2014**, *266*, 488.

[31] A. Noori, M. F. El-Kady, M. S. Rahmanifar, R. B. Kaner, M. F. Mousavi, *Chem. Soc. Rev.* **2019**, *48*, 1272.

[32] a) B. Hou, D. Benito-Alifonso, R. Webster, D. Cherns, M. C. Galan, D. J. Fermín, *J. Mater. Chem. A* **2014**, *2*, 6879; b) B. Hou, D. Benito-Alifonso, N. Kattan, D. Cherns, M. C. Galan, D. J. Fermín, *Chem. - Eur. J.* **2013**, *19*, 15847.

[33] A. S. A. Khiar, A. K. Arof, *Ionics* **2010**, *16*, 123.

[34] X. Li, J. Shao, S.-K. Kim, C. Yao, J. Wang, Y.-R. Miao, Q. Zheng, P. Sun, R. Zhang, P. V. Braun, *Nat. Commun.* **2018**, *9*, 2578.

[35] D. P. Dubal, N. R. Chodankar, D.-H. Kim, P. Gomez-Romero, *Chem. Soc. Rev.* **2018**, *47*, 2065.

[36] L. Kou, T. Huang, B. Zheng, Y. Han, X. Zhao, K. Gopalsamy, H. Sun, C. Gao, *Nat. Commun.* **2014**, *5*, 3754.

[37] a) Y. V. Skrypnyk, V. M. Loktev, *Phys. Rev. B* **2010**, *82*, 085436; b) T. Fujimori, K. Urita, Y. Aoki, H. Kanoh, T. Ohba, M. Yudasaka, S. Iijima, K. Kaneko, *J. Phys. Chem. C* **2008**, *112*, 7552.